Mechanical loading regulates organization of the actin cytoskeleton and column formation in postnatal growth plate

Christy H. Killion[†], Elizabeth H. Mitchell[†,‡], Corey G. Duke, and Rosa Serra*
Department of Cell, Developmental, and Integrative Biology, University of Alabama at Birmingham, Birmingham, AL 35294

ABSTRACT Longitudinal growth of bones occurs at the growth plates where chondrocytes align into columns that allow directional growth. Little is known about the mechanisms controlling the ability of chondrocytes to form columns. We hypothesize that mechanical load and the resulting force on chondrocytes are necessary during active growth for proper growth plate development and limb length. To test this hypothesis, we created a mouse model in which a portion of the sciatic nerve from one hind limb was transected at postnatal day 8 to cause paralysis to that limb. At 6 and 12 wk postsurgery, the hind limb had significantly less bone mineral density than contralateral controls, confirming reduced load. At 8 and 14 wk postsurgery, tibiae were significantly shorter than controls. The paralyzed growth plate showed disruptions to column organization, with fewer and shorter columns. Polarized light microscopy indicated alterations in collagen fiber organization in the growth plate. Furthermore, organization of the actin cytoskeleton in growth plate chondrocytes was disrupted. We conclude that mechanical load and force on chondrocytes within the growth plate regulate postnatal development of the long bones.

INTRODUCTION

Genetic, biochemical, and mechanical factors are all involved in determining size and shape of the limb through endochondral bone formation. Endochondral bone formation begins with an aggregation of mesenchymal cells, leading to formation of cartilage that will later be replaced with bone to form the majority of the skeleton. Postnatal longitudinal bone growth occurs through the growth plate (GP). The GP is organized into columns of chondrocytes that represent a continuum of proliferation and differentiation. Whereas the magnitude of bone lengthening depends on cell proliferation, matrix deposition, and cell enlargement during hypertrophy (Dodds, 1930; Hunziker, 1994; Wilsman et al., 1996; Li et al., 2015), chondrocyte columnar structure allows for the direction of growth. Columns form through a process called chondrocyte rotation (Dodds, 1930). During chondrocyte rotation, cells divide in a plane parallel to the long axis of the bone. Daughter cells flatten and rotate 90° on top of each other such that the long axis of the cells lies perpendicular to the long axis of the bone. Short columns eventually intercalate to form longer columns in a process similar to convergent extension. Little is known about the cellular mechanisms directing chondrocytes to form columns, but mice deleted for several regulators of actin cytoskeleton/cellular adhesion demonstrate disorganized columns that are indicative of defects in chondrocyte rotation (Aszodi et al., 2003; Terpstra et al., 2003; Wang et al., 2007; Suzuki et al., 2015).

Mechanical force is important in fetal bone development, as demonstrated in experiments using a zebrafish paralysis model and muscle-less Spd mice. These experiments indicated a specific connection between mechanical force and column intercalation (Shwartz et al., 2012). Similarly, paralysis of chick embryos resulted in decreased length of bones and decreased ossification

(Nowlan *et al.*, 2008). A role for mechanical force on postnatal skeletal development is apparent in clinical manifestations of children who experience hemiplegia resulting in unequal force on developing limbs (Roberts *et al.*, 1994). A large proportion of children with paralysis in one leg as a result of poliomyelitis demonstrated significant limb length discrepancy, with the paralyzed limb being shorter than the other limb (Ratliff, 1959). Similar leg length discrepancies, as well as severe osteopenia, were noted in children with hemiplegic cerebral palsy (Walsh *et al.*, 2000; McKenna *et al.*, 2002; Riad *et al.*, 2010; Ward *et al.*, 2016). An age-dependent effect of force on postnatal limb development, indicating a critical developmental window in which force regulates GP function, was shown in mice during spaceflight, as well as in rats unloaded by tail suspension (Duke *et al.*, 1985; Duke *et al.*, 1990; Montufar-Solis *et al.*, 2001; Park *et al.*, 2012). These results highlight the importance of force on postnatal GP function.

We developed a mouse model of hemiplegia that can be used to study the loss of mechanical force on limb development during the peak phase of bone elongation and used it to begin to determine the mechanism of how mechanical force affects postnatal GP development. Paralysis of one hind limb before the peak phase of growth in the mouse resulted in reduced bone mineral density, which confirmed reduced loading on the limb. Ultimately, the lengths of tibiae were reduced in the paralyzed hind limb relative to controls. We observed alterations in chondrocyte proliferation and differentiation. We also saw changes in collagen fibril organization in the GP after unloading. In addition, column formation was significantly disrupted and the actin cytoskeleton was reorganized in unloaded chondrocytes, suggesting that reduced tibia length could be due in part to subsequent alterations in chondrocyte rotation and directional growth of the tissue. We conclude that mechanical loading is required for organization of the actin cytoskeleton and formation of chondrocyte columns, possibly through regulation of cell rotation, in postnatal GP, contributing to overall bone length.

RESULTS AND DISCUSSION
Altered mechanical loading results in short limbs
To test the consequences of alterations in mechanical loading on endochondral bone formation during the most active stage of growth, we used sciatic nerve transection to paralyze one hind limb in mice at postnatal day 8 (P8), soon after the mice become ambulatory. This study time frame is applicable to pediatric conditions involving hemiplegia or other forms of altered loading during growth. Sciatic nerve transection procedures used previously to study muscle atrophy were adapted for this study (Kodama *et al.*, 1999). The nerve on the right side of the mouse was routinely severed and the left side was left intact and used as the contralateral (CL) control. Normal control mice that had not undergone surgery were used as nonsurgery controls. Mice naturally walk on widespread toes and walking pads located at the front of the foot (Clarke and Still, 2001). After surgery, mice lost the ability to separate their toes and control how they stood on the paralyzed hind limb. This can be seen in ink tracings of mice paws compared with control mice that had not undergone surgery (Figure 1, A and B). To quantify the disruption in gait, we used the Foot Misplacement Test to record how well mice freely walked across a raised ladder. Mice that had not undergone surgery mastered the task well, whereas mice that had undergone surgery to paralyze one limb struggled, with an average of three times more hind limb missteps than controls (Figure 1C). Changes in the gait suggest that the load was altered after surgery.

We then looked at bone mineral density using dual-energy x-ray absorptiometry (DXA) scan in the whole hind limb as well as in the tibia alone to confirm that loading was reduced on the affected limb (Figure 1, D and E). The importance of mechanical load in maintaining bone mineral density is well known (Duke *et al.*, 1985; Duke *et al.*, 1990; Montufar-Solis *et al.*, 2001; Park *et al.*, 2012). After sciatic nerve surgery, mice demonstrated a significant loss of bone mineral density in the paralyzed limb at both 6 and 12 wk postsurgery compared with control (Figure 1, D and E). The loss of bone density indicates that mechanical load was reduced in paralyzed limbs.

We hypothesized that mechanical load due to walking would be essential to promote proper development and growth of limbs in young mice. At extended times after paralysis (8 and 14 wk), mice demonstrated limb length discrepancies, with the tibiae of paralyzed, unloaded limbs (UNL) being shorter than that of nonparalyzed CL limbs (Figure 1F). At 8 wk after surgery, the UNL tibia was an average of 17% shorter than the CL control, whereas at 14 wk, the UNL tibia was an average of 9% shorter than controls. Bones in the limbs halt their growth after puberty, which can result in lifelong conditions. Differences in limb lengths as small as 4% have been shown to cause back pain in adults (Knutson, 2005). Children with >5.5% difference in limb lengths demonstrated gait compensations that would be expected to lead to secondary pathologies later in life (Aiona *et al.*, 2014). Therefore the magnitude of the discrepancy shown here is well greater than what would be expected to result in secondary skeletal problems (Walsh *et al.*, 2000; Aiona *et al.*, 2014). There was no difference between tibiae length in normal control mice that had not undergone surgery compared with the contralateral limb in mice that had undergone the surgery. Next we imaged the shape of the bones using micro–computed tomography (μCT; Figure 1G). The length of the bone from the cranial tip of the epiphysis to the tibial inflection was measured from the reconstructed images (Figure 1H). The length of the UNL tibia was less than the CL, confirming the whole-bone measurements. In addition, the width of the UNL bone across the GP was significantly increased relative to the CL (Figure 1I). The results support the hypothesis that altered loading during the active phase of growth in mice causes disruptions to endochondral bone formation that lead to shortened limbs.

Altered mechanical loading during postnatal growth results in reduced proliferation and hypertrophic differentiation
Chondrocytes in the GP form columns of cells that proliferate and differentiate to increase the length of the bone. Reduced mechanical load during embryonic development, due to loss of muscle function, resulted in reduced proliferation and hypertrophy of GP chondrocytes in fish, chick, and mouse embryos (Rot-Nikcevic *et al.*, 2006; Gomez *et al.*, 2007; Nowlan *et al.*, 2010; Sharir *et al.*, 2011). Models of postnatal development, including spaceflight and tail suspension, also demonstrated reduced proliferation and hypertrophic differentiation in unloaded GPs (Montufar-Solis *et al.*, 2001; Park *et al.*, 2012). To begin to determine the mechanism of limb shortening in response to reduced loading through postnatal paralysis, we compared proliferation in prehypertrophic chondrocytes from UNL and CL limbs. Proliferation was measured with Ki67 staining (red), a marker of proliferative cells, and 4′,6-diamidino-2-phenylindole (DAPI; blue) to mark the nucleus (Figure 2A). Alterations in the percentage of Ki67-positive cells were not detected in mice 1 wk postsurgery; however, there was a significant decrease in the percentage of Ki67-positive cells in UNL GPs relative to controls 2 wk postsurgery (Figure 2B). We did not detect changes in prehypertrophic cell density between CL control and UNL samples (1 wk: CL mean, 456 cells/2547 × 600 pixels, SEM = 28.54; UNL mean, 421, SEM = 44.43; $N = 3$, $p = 0.6737$; 2 wk: CL mean, 402,
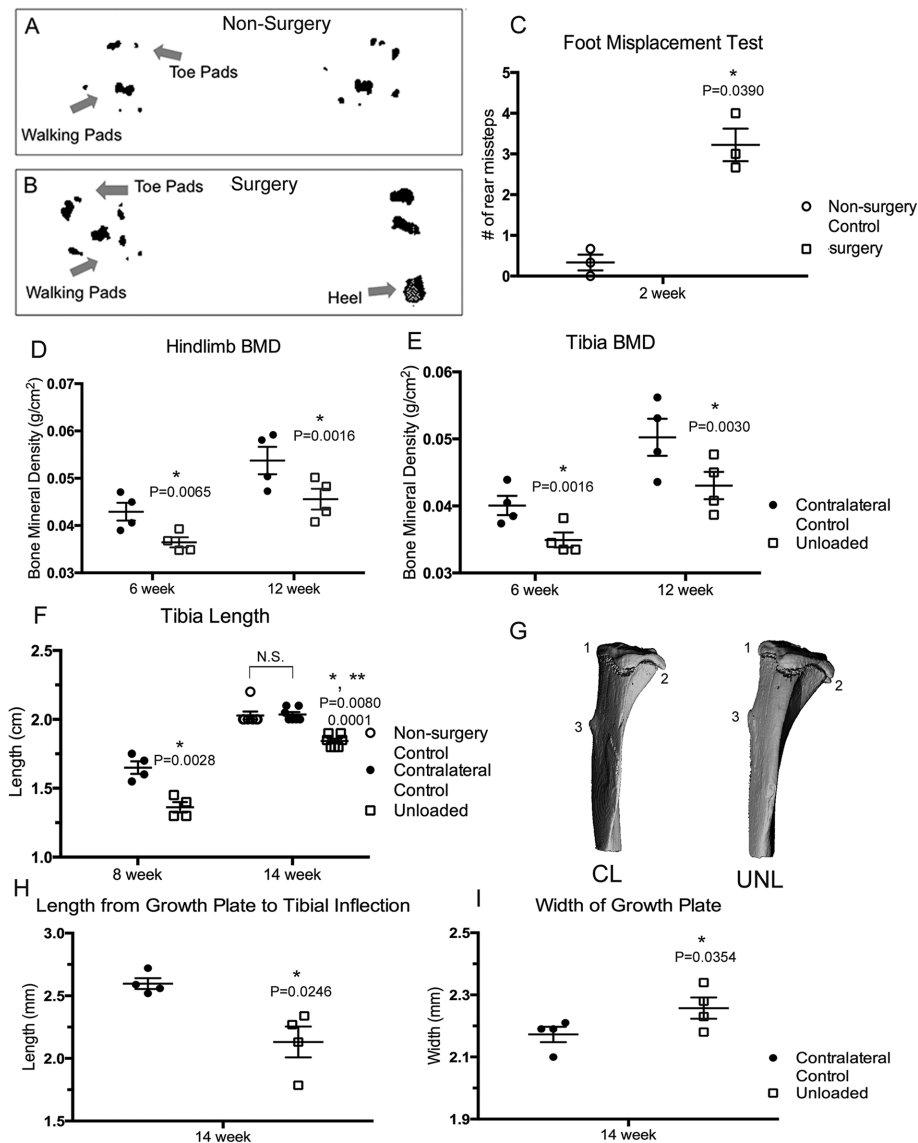
FIGURE 1: Sciatic nerve dissection causes partial paralysis and unloading. (A) Ink footprints from hind paws of nonsurgery control mouse show clear toe pad prints for both feet, whereas the mouse that underwent sciatic nerve surgery (B) shows clear toe pad prints for the left foot, but the right foot shows no separation of toes and the addition of a heel print. (C) Gait for the mouse was tested using the Foot Misplacement Test; t test, $N = 4$ for surgery mice, and $N = 3$ for nonsurgery controls. (D, E) Mice were scanned using DXA at 6 and 12 wk postsurgery; paired t test ($N = 4$). (F) Lengths of unloaded and contralateral control tibiae were compared in mice 8 ($N = 4$) and 14 wk ($N = 7$) postsurgery. Length of the tibiae from mice at 14 wk after surgery was also compared with nonsurgery controls ($N = 6$). *Paired t test, **unpaired t test. (G) Representative μCT images of proximal tibia from CL control and UNL limbs. The three points used for measurements are 1) cranial tip of the proximal epiphysis, 2) caudal tip of the medial condyle, and 3) cranial point of the inflection on the tibial tuberosity. (H) Length of the growth plate to the tibial inflection (points 1–3). (I) Width of the growth plate (points 1 and 2). $N = 4$, paired t test.

the GP that expressed collagen type X was significantly decreased in UNL for both 1 and 2 wk compared with CL controls (Figure 2D). Reduced proliferation and hypertrophic differentiation could account in part for a decrease in total limb length.

Altered loading results in disorganization of columnar structure of the GP and alterations in collagen fibers in the cartilage matrix

Without columnar structure in the GP, growth in the limb would not be directional, and proper length and shape of skeletal elements would be disrupted (Romereim and Dudley, 2011). Disruptions to column organization in the prehypertrophic zones of the GP could be seen as early as 1 wk postsurgery in hematoxylin and eosin (H&E)–stained sections from UNL and CL tibiae (Figure 3, A–D). More dramatic disruptions to column organization were observed at 2 wk postsurgery (Figure 3C). Unloaded chondrocytes arranged into small clusters rather than longer columns seen in the prehypertrophic zones of CL GPs. To quantify column organization in the GP, we developed a plug-in for FIJI/ ImageJ (Schindelin et al., 2012) to measure GP column index (CI) and the percentage of prehypertrophic cells in columns (Supplemental Document S1). Column requirements were adapted from Randall et al. (2012). In control GPs, CI and percentage of cells in columns dramatically increased between 2 and 3 wk of age, equal to 1 and 2 wk postsurgery, indicating that this is a critical time of organization in the postnatal GP (Figure 3, E and F). GPs from UNL limbs did not demonstrate this strong organization into columns and showed significant decreases in CI (Figure 3E) and percentage of cells in columns (Figure 3F) at 1 and 2 wk after paralysis. Furthermore, the prehypertrophic cells in the UNL limbs were slightly but significantly rounder than those cells in the CL limbs as measured by the cellular aspect ratio (length over height, where 1.0 would be a perfectly round cell). The average aspect ratio for the CL cells at 1 wk was 3.456 (SEM = 0.2495). The ratio for the UNL was 2.916 (SEM = 0.2278; $N = 5$, $p = 0.0029$). At 2 wk, the CL ratio was 2.672 (SEM = 0.0509) and the UNL ratio was 2.424 (SEM = 0.0995;

$N = 5$, $p = 0.0476$). We also used paralysis via Botox injection as a second method to alter loading in the hind limb (Grimston et al., 2007). Paralysis was confirmed in these mice by observing alterations in the gait and ability to unfurl toes (unpublished data). In contrast to the sciatic nerve surgery, the gait of injected mice began to normalize around 1 wk postinjection. Therefore mice injected with Botox were characterized only at 1 wk after injection. CI and percentage of cells in columns were also altered after Botox

SEM = 19.14; UNL mean, 444, SEM = 18.76; $N = 3$, $p = 0.2930$). Differences in the percentage of prehypertrophic cells that express the apoptosis marker cleaved caspase 3 were not detected (1 wk: CL mean, 30.33%, SEM = 3.18; UNL mean = 28%, SEM = 7.77; $N = 3$, $p = 0.7948$; 2 wk: control mean, 19.67%, SEM = 5.04; Surgery mean, 13.33%, SEM = 3.71; $N = 3$, $p = 0.1132$), suggesting the cells in the UNL GP were viable. We then used collagen type X staining to measure hypertrophic differentiation (Figure 2C). The percentage of
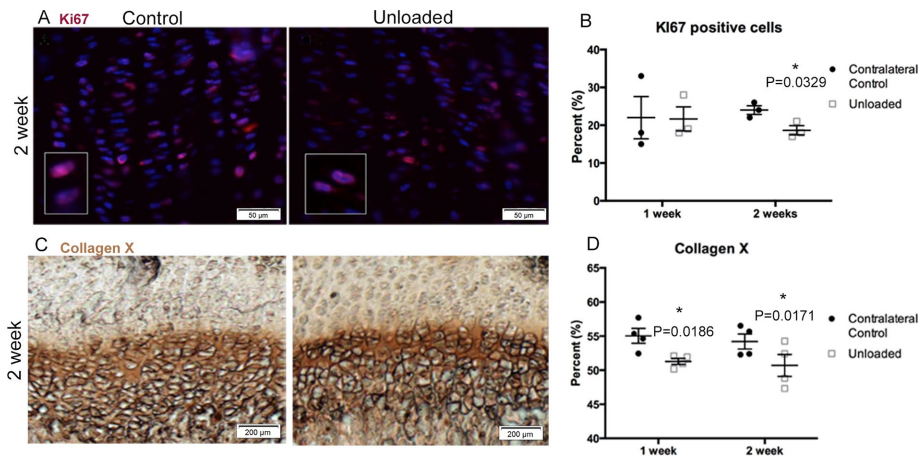
FIGURE 2: Proliferation and maturation are reduced in GP chondrocytes in unloaded limbs. (A) Immunofluorescence staining of Ki67 (red) and DAPI (blue) in the contralateral control (left) and unloaded tibia (right) 2 wk after surgery. (B) The percentage of Ki67-expressing cells in the GP (1 wk, $N = 3$; 2 wk, $N = 3$). (C) Immunohistological staining for collagen X in the contralateral GP (left) and unloaded GP (right) 2 wk after surgery. (D) Percentage area of the total GP expressing collagen X was determined for 1 wk ($N = 3$) and 2 wk ($N = 3$) after surgery. Paired t tests.

injections (CI: CL mean, 24.5782, SEM = 6.102; Botox mean, 14.4391, SEM = 4.4344; $N = 3$, $p = 0.0455$; percentage of cells in columns: CL mean, 39, SEM = 5; Botox mean, 25, SEM = 4; $N = 3$, $p = 0.0054$). The results suggest that loading is required for proper column formation during critical stages of postnatal endochondral bone formation.

The mechanical properties of transverse septa (horizontal septa between cells in the column) and longitudinal septa (vertical, between columns) measured by atomic force microscopy during development of the GP were recently described (Prein *et al.*, 2016). It was hypothesized that the stiffness of the septa was related to column formation. To determine whether the organization of collagen fibers was disrupted after unloading, we stained sections from CL and UNL limbs with Picosirius red and followed with polarized light microscopy, a common method to study collagen networks in tissues (Figure 4; Junqueira *et al.*, 1979). Transverse septa were visible in sections from CL mice 2 d after surgery. Differences in staining between CL and UNL were not detected 2 d after unloading ($n = 3$; Figure 4, A and B). At 1 wk after surgery, CL GP showed collagen fibers in the longitudinal septa along the entire length of the GP (Figure 4C). At 2 wk after surgery (3 wk of age), the transverse and longitudinal septa were well defined, with sharp fibers visible in the CL GP (Figure 4E). At 1 and 2 wk after unloading, alterations in the transverse and longitudinal septa were observed (Figure 4, C–F). Most notably, longitudinal septa were discontinuous and did not extend the entire length of the GP. Sharp collagen fibers were not easily detected. The results suggest that unloading has an effect on the organization of collagen fibers in the cartilage matrix; however, it is not known whether this is a consequence of cells failing to form columns or whether the collagen fibers directly regulate column formation.
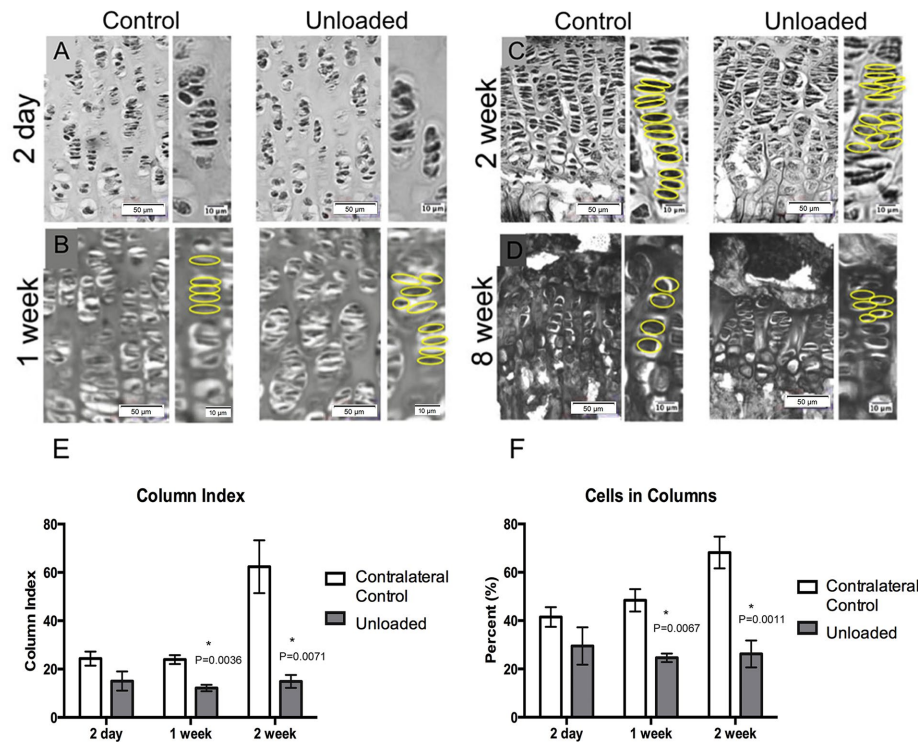
Unloading alters cytoskeletal organization in chondrocytes

The biomechanical signals that regulate GP organization are not known; however, the actin cytoskeleton is known to be important for GP function (Feng and Walsh, 2004; Krakow *et al.*, 2004; Nurminsky *et al.*, 2007). Deletion of Cdc42 or Rac1, GTPase regulators of actin dynamics, in Col2a-expressing chondrocytes results in loss of columnar organization suggestive of defects in chondrocyte rotation (Woods *et al.*, 2007; Suzuki *et al.*, 2015). It is known that this family of GTPases is regulated by integrins, including β1 integrin. A conditional loss of β1 integrin in the GP also results in disorganized actin cytoskeleton and defects in chondrocyte rotation, resulting in disorganized columns (Aszodi *et al.*, 2003). Ablation of integrin-linked kinase also results in disruptions to columnar organization (Terpstra *et al.*, 2003). We previously showed that primary cilia (PC) are required for column formation in postnatal mice (Song *et al.*, 2007). Chondrocytes in PC-deleted mice demonstrated

FIGURE 3: GP organization is disrupted in the unloaded limbs. (A) H&E staining of GPs from unloaded (right) and paired contralateral control tibia (left) 2 d after surgery, (B) 1 wk after surgery, (C) 2 wk after surgery, and (D) 8 wk after surgery to show column structure in the prehypertrophic zones. The hypertrophic zone is visible in the 2- and 8-wk samples for context. Right, higher-magnification images showing a representative column of chondrocytes; yellow circles highlight individual chondrocytes. (E) Column index at 2 d ($N = 5$), 1 wk ($N = 5$), and 2 wk ($N = 5$) after surgery. (F) Percentage of cells in columns under each condition. Paired t test.
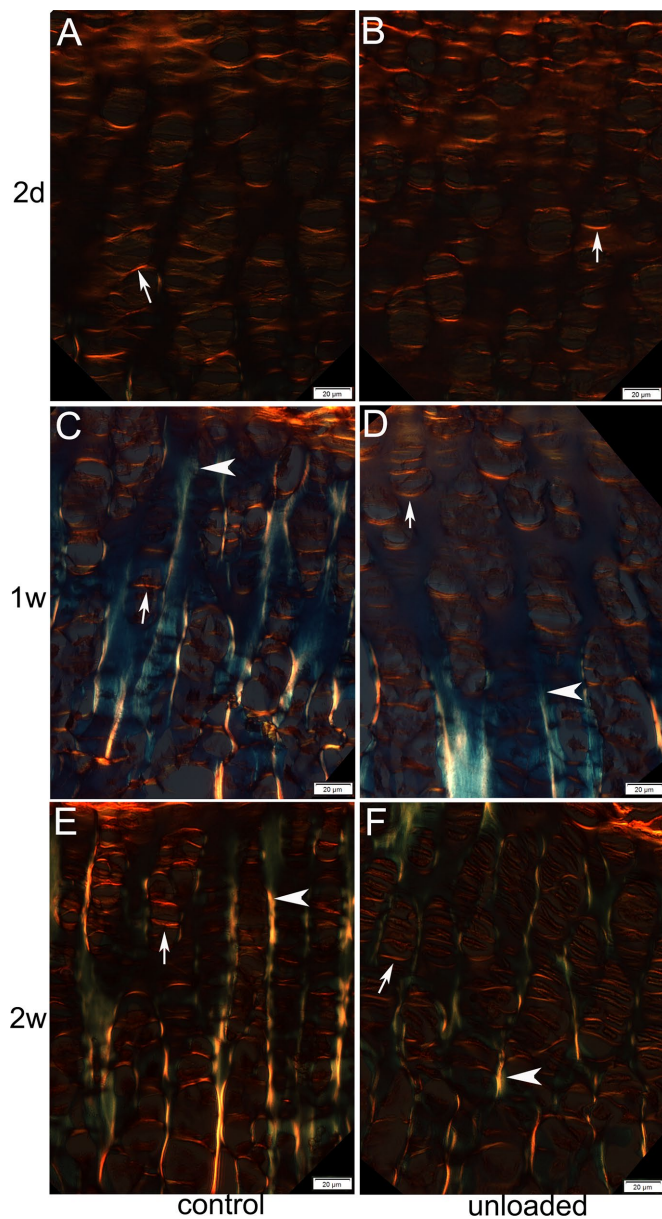
FIGURE 4: Collagen fiber organization is disrupted in unloaded growth plate. Sections from proximal tibia from contralateral control (A, C, E) and unloaded (B, D, F) limbs were stained with Picosirius red and visualized under polarized light microscopy. Collagen fibers are seen in red, yellow, or green. Representative transverse septa (arrow) and longitudinal septa (arrowheads) are marked.

organized into short, thick fibers throughout the cell, whereas the cells in the control samples demonstrated primarily cortical actin staining (Figure 5, C–F and G–J). The results indicate that loading affects actin organization in GP chondrocytes.

In summary, we showed that unloading limbs in actively growing mice results in reduced tibia length, reduced proliferation and hypertrophic differentiation, and disorganization of the columnar structure in the GP, as well as in alterations in the actin cytoskeleton. It has been shown that actin filaments can directly sense changes in tension, leading to reorganization of the actin cytoskeleton (Hayakawa *et al.*, 2011; Galkin *et al.*, 2012). We hypothesize that reduced mechanical load on the GP results in reorganization of the actin cytoskeleton in response to altered tension on the cell. Reorganization of the actin cytoskeleton could then disrupt columnar organization in the growth plate through alterations in chondrocyte rotation, subsequently contributing to defects in length and shape of long bones. Future experiments will identify the pathways used to sense force on chondrocytes and provide novel therapeutic approaches to the treatment of various limb length disorders, as well as a broader understanding of the necessity of mechanical load in endochondral bone formation.

MATERIALS AND METHODS
Mouse models
C57/Bl6 (Envigo) mice were used except where noted. All mice in this study were maintained following the guidelines of the Institutional Animal Care and Use Committee of the University of Alabama at Birmingham.

Botox paralysis and surgical method of unloading
Mice at P8 were anesthetized with one short-term exposure to 32% isoflurane. Botox (onabotulinumtoxinA; Allergan) was diluted in sterile saline to 6 U/100 µl and injected into the right intramuscular hindlimb. A total of 2.4 U was injected in four separate 10-µl injections as follows: two in the quadriceps, one in the hamstring, and one in the posterior calf, using a Hamilton syringe (8920; Hamilton). Paralysis was confirmed by observation. Mice were killed 1 wk after Botox injections.

Mice at P8 were anesthetized using short-term exposure to 32% isofluorane and continual exposure to 2–5% isofluorane. The right hind limb of each mouse was prepared for surgery by removing the hair and sanitizing with Betadine and 70% isopropyl alcohol. The sciatic nerve bundle connects the spine to the hind limb. During sciatic nerve surgery, we took care to ensure that sciatic nerve transection occurred proximal to the bifurcation so that the hind limb was paralyzed, including the metatarsals, tibia, and majority of the femur. The sciatic nerve was transected as described in Kodama *et al.* (1999). Surgery was performed through an incision that exposed the sciatic nerve proximal to the bifurcation. The incision was closed with Vetbond (3 M Vetbond Tissue Adherent #1469SB). Mice were killed 2 d and 1, 2, 6, 8, and 14 wk postsurgery. We confirmed by visual inspection that the portion of the sciatic nerve that was severed did not grow back or reattach postsurgery.

Ink footprints
Hind paws from mice 2 wk after surgery (N = 4) and nonsurgery control mice (N = 3) were painted with black calligraphy ink (22744; Winsor & Newton). Mice were placed on a blank white sheet of paper and allowed to walk freely. Representative images of hindpaw ink prints were chosen for the nonsurgical control mice and mice that had undergone surgery.

alterations in the localization of focal adhesion kinase (FAK) and organization of the actin cytoskeleton. It is not known how the cytoskeleton functions to organize the GP, but the actin cytoskeleton has been shown to sense changes in tension and compression of chondrocytes in culture (Haudenschild *et al.*, 2008). Therefore we hypothesized that altered loading would affect the actin cytoskeleton in GP chondrocytes. To test this hypothesis, we stained GPs from UNL and CL limbs with rhodamine-conjugated phalloidin to visualize F-actin in the GP (Figure 5). Unloading resulted in increased phalloidin staining, as well as a change in the organization of the cytoskeleton by 2 d after surgery (Figure 5, A and B). At 1 and 2 wk after surgery, the actin cytoskeleton in the UNL GP was
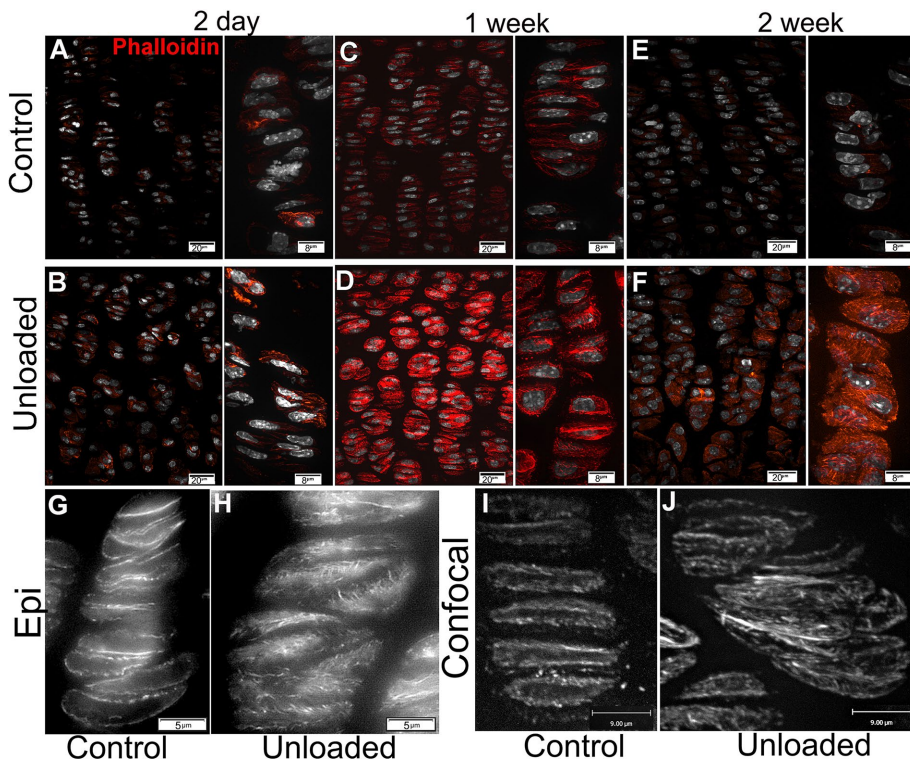
FIGURE 5: Unloading disrupts actin cytoskeleton organization. The z-stack images from confocal microscopy of phalloidin staining for F-actin (red) and DAPI staining of nuclei (pseudocolored white) in tibia from unloaded (B, D, F) and contralateral (A, C, D) limbs at 2 d postsurgery (A, B; N = 3), 1 wk postsurgery (C, D; N = 4), and 2 wk postsurgery (E, F; N = 4). Right, higher-magnification images of chondrocytes in the prehypertrophic zones. Images in A–F were acquired with the same exposure settings. (G–J) To see more clearly the actin fiber organization and normalize for the amount of actin, images of phalloidin-stained sections were acquired in grayscale using automatic exposure settings. Two weeks after surgery, control (G, I) and unloaded (H, J) epifluorescence images (G, H) and confocal z-stacks (I, J).

Foot misplacement test

At 2 wk, surgery (N = 4) and nonsurgery (N = 3) mice were placed on a raised ladder, and infrared lasers noted missteps and missed rungs of the ladder. Each mouse was allowed to traverse the ladder three separate times. Missteps by rear feet were quantified and averaged for each group. Statistical analysis was performed using the Student's t test.

DXA and quantification

DXA (Lunar, PIXImus) images were performed on mice 6 and 12 wk after surgery (N = 4). DXA uses two x-rays of differing intensity to allow for the rapid determination of fat, soft-lean tissue, and bone (bone mineral content and density) in vivo in small rodents. Mice were anesthetized with continual exposure to 2–5% isoflurane for the duration of the scan. Scans were performed to optimized conditions as cited in Nagy and Clair (2000). Bone density was determined for each total hind limb and tibia (contralateral and unloaded). Bone density was compared using the paired t test.

Tibia measurements and quantification

Long bones from the 8- and 14-wk surgery mice were dissected to include the foot and a portion of the femur. The fibula was removed, and the remaining bone was cleaned of excess muscle and fat and placed in a Petri dish containing a centimeter ruler. The femur was placed perpendicular to the ruler above the start of the dashes, and the length of the tibia was measured from below the patella to the calcaneum/heel of the mouse and recorded in centimeters. The surgery length (N = 3 and 7) was compared with the contralateral control length (N = 3 and 7) for 8- and 14-wk mice, respectively, and to the nonsurgical control length (N = 7) for 14-wk mice. Significance was determined using paired t tests for the comparison between unloaded limbs and contralateral control limbs, and an unpaired t test was used to compare nonsurgery mice with 14-wk contralateral control limbs.

µCT scanned images

Excised tibiae from mice were scanned using the Scanco µCT40 desk-top cone-beam µCT scanner (µCT Tomography, version 5.44; Scanco Medical, Brüttisellen, Switzerland). Scans were automatically reconstructed into two-dimensional slices, and all slices were analyzed using the µCT Evaluation Program (version 6.5-2; Scanco Medical). The scan was performed to image the whole tibia. Tibiae were placed horizontally in a 16-mm scanning holder and scanned at the following settings: 16-µm resolution, 250 projections/180°, 70 kV$_p$, 114 µA, with an integration time of 200 ms. The scan started above the sample and continued to include the whole tibia. The region of interest (tibia) was outlined in all slices that contained bone. The threshold of 200 was used to distinguish bone, and data were obtained on bone volume and density. Three-dimensional (3D) reconstruction (µCT Ray, version 3.8) was performed using all of the outlined slices.

µCT measurements

The 3D reconstruction scans were printed on graph paper. On each image, three main points were noted. The cranial tip of the proximal epiphysis was labeled as point 1. The caudal tip of the medial condyle of the proximal epiphysis was labeled as point 2. The cranial point of the inflection on the tibial tuberosity was labeled as point 3. The length of the growth plate to tibial inflection was measured by connecting points 1 and 3 vertically. The vertical line was measured with a caliper and recorded in millimeters. The width of the growth plate was measured by connecting points 1 and 2. The horizontal line was measured with a caliper and recorded in millimeters.

Cryoembedding and sectioning

Tibiae were removed and fixed in 4% paraformaldehyde (PFA) at 4°C overnight. Tibiae were pretreated with 5 mg/ml sodium borohydride (213462-25G; Sigma-Aldrich) following the protocol from Ahrens and Dudley (2011) for cryotissue preparation embedding. Tibiae were placed in 30% sucrose in 1× phosphate-buffered saline (PBS) overnight, equilibrated with Optimal Cutting Temperature (O.C.T.) compound (Sakura, Torrance, CA) and flash frozen in a mold filled with O.C.T. Sections were cut with a cryostat at 10 µm in the coronal plane.

Histology

Cryosections were stained with H&E. After rehydration, slides were rinsed in deionized H_2O for 3 min, stained in hematoxylin (SH26; Sigma-Aldrich) for 1 min, washed in tap H_2O for 5 min, quickly dipped in 0.25% acid ethanol, rinsed in tap H_2O, stained in eosin (HT110132; Sigma-Aldrich) for 3 min, and finally dehydrated through 100% ethanol and xylene and coverslipped with Cytoseal60. H&E images were used in the multiple tests, including the column index, the cells in column analysis, and the aspect ratio analysis.

Column measurements

FIJI software was used to analyze H&E-stained samples for the column index and the cells in column measurements. We cropped 20× images to a region of 1800 × 600 pixels and centered them on the proliferative zone of the growth plate. The macro Calculate Angle from Segmented Line.ijm (Supplemental Document S1) was then loaded into FIJI and used for the remainder of the analysis. Segmented lines were drawn between chondrocytes by clicking on each individual cell that fit the parameters of being in a column as followed and adapted from Randall *et al.* (2012). The qualifications to be classified as a column were as follows: 1) a column must include at least three cells with 2) the angle between each cell ranging from −155 to −179° or 155 to 180°, and 3) the cells cannot be >20 pixels apart. Running the macro caused three windows to popup: the results window, a "number of cells in column" window, and a log window. The results window kept track of the length of column metric, the number of cells in column window showed the number of cells clicked on, and the log window showed the angle measurements for individual chondrocytes in each segmented line. Second, total cells were counted with the ImageJ cell counter plug-in, and using the number of cells window and total cells counted, the percentage of cells in columns was calculated. The CI was then calculated as the percentage of cells in columns multiplied by the average column length recorded from the results window of calculate angle from segmented line macro. The columns were calculated on one 20× image per biological replicate. Biological replicates were sections from separate mice at 2 d ($N = 5$) and 1 wk ($N = 5$) and 2 wk ($N = 5$) after surgery as well as Botox paralysis ($N = 3$). Aspect ratio was calculated by selecting a 400 × 400 pixel square of the proliferative zone. Ovals were drawn around the cell, and the measurements were taken to calculate the aspect ratio via the measure tool from FIJI. Cells were counted both inside and outside of the columns, with $N = 5$ for all conditions.

Sirius red staining

Collagen fiber density and organization were viewed using Sirius red staining. Before the stain, a solution of 0.5 g of Sirius red F3B, also known as Direct Red 80 (36-554-8; Sigma-Aldrich) was added to 500 ml of saturated picric acid solution (SP9200-100; Fisher Scientific) for a total solution of 0.1% Direct Red stain. The cryosections were brought to room temperature and rehydrated with 1× PBS. They were then submerged in the Direct Red stain solution for 1 h at room temperature under a chemical hood. Slides were dipped for 5 min two times in a solution of acidified water (5 ml of glacial acetic acid to 1 l of water). The water solution was vigorously removed from the sections, which were dehydrated through three changes in 100% ethanol (UN1170; Decon Laboratories) and cleared in xylene (X5P-1Gal; Fisher Scientific). The slides were mounted with Cytoseal 60 (8310-4; Thermo Scientific) mounting medium. Slides were visualized with polarized light (Olympus BX-50 microscope) at the same angles for each sample.

Immunofluorescence staining for Ki67, caspase 3, and actin

Cryosections were rehydrated in 1× PBS and then fixed in ice-cold methanol for 20 min. Sections were blocked for 1 h with 0.1% Triton X-100, 5% bovine serum albumin (BSA), 5% normal goat serum (S-1000; Vector Labs). Primary antibody anti-Ki67 (1:400 dilution; ab15580; Abcam) or cleaved caspase 3 (1:1000 dilution; 9662; Cell Signaling Technology) was incubated overnight at 4°C. Sections were incubated with secondary antibodies anti–rabbit Alexa Fluor 546 (1:1000 dilution; A11010; Life Technologies) for 3 h at room temperature in 1% BSA solution. Phalloidin-594 (A12381; Life Technologies) was stained at 1:500 dilution for 1 h at room temperature. Nuclei were stained with 1:500 DAPI (62248; Thermo Fisher Scientific) for 5 min.

Ki67 and caspase 3 quantification

Quantification of Ki-67 and caspase 3 staining were completed using FIJI. We cropped 40× images to 2547 × 800 pixels and centered them on the proliferative zone of the growth plate. An identical threshold was set for the red channel, which contained the Ki67 or caspase 3 stain. Images were then switched to binary, and watershed was applied to separate touching objects. Particles were counted that had an area >100 and <1000 pixels. For nuclei counting, an identical threshold was set for the blue channel; images were also switched to binary and a watershed applied. Particles were counted that had an area >100 and <1000 pixels. Individual cell counting was used as needed to count nuclei not separated through the watershed function. Ki-67 staining is presented as a percentage of the total number of positive cells. Caspase 3 staining was calculated as the percentage of the total number of positive cells over the total number of cells. Cell density for Ki67 stain was determined through the total cell count of the nuclei. The 1- and 2-wk surgery limbs ($N = 3$) were compared with contralateral control limbs ($N = 3$) and tested for significance using the paired t test.

Immunohistochemistry staining and quantification of type X collagen

Cryosections were rehydrated in 1× PBS and fixed with 4% PFA for 10 min at room temperature. Sections were pretreated with 0.2 mg/ml proteinase K stock concentration (1:100 dilution) for 5 min at room temperature. Sections were then blocked for 1 h with 5% BSA and 5% normal goat serum in 1× Tris-buffered saline/Tween 20 (TBST). Primary antibody to collagen X (1:1000 dilution; ab58632; Cell Signaling) in 1% BSA in 1× TBST was incubated on the sections at 4° overnight. Goat anti–rabbit immunoglobulin horseradish peroxidase–linked secondary (1:1000 dilution, sc-2004; Santa Cruz Biotechnology) was placed on sections for 1 h at room temperature. Sections were washed and then stained using the DAB substrate following the instructions in the ImmPACT DAB Kit (SK-4105; Vector Laboratories). Sections were mounted with Cytoseal 60.

The hypertrophic zone was measured by the chondrocytes expressing collagen X using FIJI. We cropped 20× images and centered them to include the entire growth plate. First, a line was drawn from the top of the resting zone to the bottom of the hypertrophic zone, and the length was measured using the Measure plug-in. Second, a line was drawn to included the collagen X–expressing cells, and the length was measured using the Measure plug-in. Eight measurements were averaged for each sample, and the results are presented as the percentage of the total growth plate that expresses collagen X. The 1- and 2-wk surgery limbs ($N = 3$) and contralateral control limbs ($N = 3$) were compared using the paired t test for significance.

Confocal imaging

Sections were imaged using a Hamamatsu C9100-50 electron-multiplying charge-coupled device camera (Hamamatsu Photonics, Hamamatsu City, Japan) on an inverted Nikon TE2000-U microscope equipped with a 40× Plan Apochromat oil-immersion objective (Nikon Instruments Melville, NY), a 100× Plan Apochromat oil-immersion objective (Nikon Instruments), and an Ultraview-ERS 6FE spinning-disk confocal module controlled by Volocity 6.2 software (PerkinElmer, Shelton, CT).

Statistical analysis

Statistical analysis was performed using a paired t test when comparing unloaded limbs to paired contralateral control samples. An unpaired t test was used to determine statistical analysis when comparing limbs from mice that had surgery to nonsurgical controls. Unless otherwise noted, for both tests, $*p > 0.05$.

REFERENCES

Ahrens MJ, Dudley AT (2011). Chemical pretreatment of growth plate cartilage increases immunofluorescence sensitivity. J Histochem Cytochem 59, 408–418.

Aiona M, Do KP, Emara K, Dorociak R, Rosemary P (2014). Gait patterns in children with limb length discrepancy. J Pediatr Orthop 35, 280–284.

Aszodi A, Hunziker EB, Brakebusch C, Fässler R (2003). Beta1 integrins regulate chondrocyte rotation, G1 progression, and cytokinesis. Genes Dev 17, 2465–2479.

Clarke KA, Still J (2001). Development and consistency of gait in the mouse. Physiol Behav 73, 159–164.

Dodds GS (1930). Row formation and other types of arrangement of cartilage cells in endochondral ossification. Anat Rec 46, 385–399.

Duke J, Janer L, Campbell M, Morrow J (1985). Microprobe analyses of epiphyseal plates from spacelab 3 rats. Physiologist 28 (6 Suppl), S217–S218.

Duke PJ, Durnova G, Montufar-Solis D (1990). Histomorphometric and electron microscopic analyses of tibial epiphyseal plates from cosmos 1887 rats. FASEB J 4, 41–46.

Feng Y, Walsh CA (2004). The many faces of filamin: a versatile molecular scaffold for cell motility and signalling. Nat Cell Biol 6, 1034–138.

Galkin VE, Orlova A, Egelman EH (2012). Actin filaments as tension sensors. Curr Biol 22, R96–R101.

Gomez C, David V, Peet NM, Vico L, Chenu C, Malaval L, Skerry TM (2007). Absence of mechanical loading in utero influences bone mass and architecture but not innervation in myod-Myf5-deficient mice. J Anat 210, 259–271.

Grimston SK, Silva MJ, Civitelli R (2007). Bone loss after temporarily induced muscle paralysis by botox is not fully recovered after 12 weeks. Ann NY Acad Sci 1116, 444–460.

Haudenschild DR, 'Lima DD, Lotz MK (2008). Dynamic compression of chondrocytes induces a rho kinase-dependent reorganization of the actin cytoskeleton. Biorheology 45, 219–28.

Hayakawa K, Tatsumi H, Sokabe M (2011). Actin filaments function as a tension sensor by tension-dependent binding of cofilin to the filament. J Cell Biol 195, 721–727.

Hunziker EB (1994). Mechanism of longitudinal bone growth and its regulation by growth plate chondrocytes. Microsc Res Tech 28, 505–519.

Junqueira LCU, Bignolas G, Brentani RR (1979). Picrosirius staining plus polarization microscopy, a specific method for collagen detection in tissue sections. Histochem J 11, 447–455.

Knutson GA (2005). Anatomic and functional leg-length inequality: a review and recommendation for clinical decision-making. Part I, anatomic leg-length inequality: prevalence, magnitude, effects and clinical significance. Chiropr Osteopath 13, 11.

Kodama Y, Dimai HP, Wergedal J, Sheng M, Malpe R, Kutilek S, Beamer W, Donahue LR, Rosen C, Baylink DJ, et al. (1999). Cortical tibial bone volume in two strains of mice: effects of sciatic neurectomy and genetic regulation of bone response to mechanical loading. Bone 25, 183–190.

Krakow D, Robertson SP, King LM, Morgan T, ET Sebald, Bertolotto C, Wachsmann-Hogiu S, Acuna D, Shapiro S, Takafuta T, et al. (2004). Mutations in the gene encoding filamin b disrupt vertebral segmentation, joint formation and skeletogenesis. Nat Genet 36, 405–410.

Li Y, Trivedi V, Truong TV, Koos DS, Lansford R, Chuong C-M, Warburton D, Moats RA, Fraser SE (2015). Dynamic imaging of the growth plate cartilage reveals multiple contributors to skeletal morphogenesis. Nat Commun 6, 6798.

McKenna J, Walsh M, Jenkinson A, Hewart P, O'Brien T (2002). Limb length discrepancy and equinus deformity in the hemiplegic cerebral palsy patient. Orthop Proc 84-B (Suppl I), 1-a-1.

Montufar-Solis D, Duke PJ, Morey-Holton E (2001). The spacelab 3 simulation: basis for a model of growth plate response in microgravity in the rat. J Gravit Physiol 8, 67–76.

Nagy TR, Clair A-L (2000). Precision and accuracy of dual-energy x-ray absorptiometry for determining in vivo body composition of mice. Obes Res 8, 392–398.

Nowlan NC, Prendergast PJ, Murphy P (2008). Identification of mechanosensitive genes during embryonic bone formation. PLoS Comput Biol 4, e1000250.

Nowlan NC, Sharpe J, Roddy KA, Prendergast PJ, Murphy P (2010). Mechanobiology of embryonic skeletal development: insights from animal models. Birth Defects Res C Embryo Today 90, 203–213.

Nurminsky D, Magee C, Faverman L, Nurminskaya M (2007). Regulation of chondrocyte differentiation by actin-severing protein adseverin. Dev Biol 302, 427–437.

Park H, Kong SY, Kim HW, Yang IH (2012). Altered cellular kinetics in growth plate according to alterations in weight bearing. Yonsei Med J 53, 618–624.

Prein C, Warmbold N, Farkas Z, Schieker M, Aszodi A, Clausen-Schaumann H (2016). Structural and mechanical properties of the proliferative zone of the developing murine growth plate cartilage assessed by atomic force microscopy. Matrix Biol 50, 1–15.

Randall RM, Shao YY, Wang L, Ballock RT (2012). Activation of Wnt planar cell polarity (PCP) signaling promotes growth plate column formation in vitro. J Orthop Res 30, 1906–1914.

Ratliff AH (1959). The short leg in poliomyelitis. J Bone Joint Surg Br 41-B, 56–69 .

Riad J, Finnbogason T, Broström E (2010). Leg length discrepancy in spastic hemiplegic cerebral palsy: a magnetic resonance imaging study. J Pediatr Orthop 30, 846–850.

Roberts CD, Vogtle L, Stevenson RD (1994). Effect of hemiplegia on skeletal maturation. J Pediatr 125, 824–28.

Romereim SM, Dudley AT (2011). Cell polarity: the missing link in skeletal morphogenesis? Organogenesis 7, 217–228.

Rot-Nikcevic I, Reddy T, Downing KJ, Belliveau AC, Hallgrímsson B, Hall BK, Kablar B (2006). Myf5 –/– :MyoD –/– amyogenic fetuses reveal the importance of early contraction and static loading by striated muscle in mouse skeletogenesis. Dev Genes Evol 216, 1–9.

Schindelin J, Arganda-Carreras I, Frise E, Kaynig V, Longair M, Pietzsch T, Preibisch S, Rueden C, Saalfeld S, Schmid B, et al. (2012). Fiji: an open-source platform for biological-image analysis. Nat Methods 9, 676–82.

Sharir A, Stern T, Rot C, Shahar R, Zelzer E, Belteki G, Haigh J, Sison K, Costantini F, Whitsett J, et al. (2011). Muscle force regulates bone shaping for optimal load-bearing capacity during embryogenesis. Development 138, 3247–3259.

Shwartz Y, Farkas Z, Stern T, Aszódi A, Zelzer E (2012). Muscle contraction controls skeletal morphogenesis through regulation of chondrocyte convergent extension. Dev Biol 370, 154–163.

Song B, Haycraft CJ, Seo H-S, Yoder BK, Serra R (2007). Development of the post-natal growth plate requires intraflagellar transport proteins. Dev Biol 305, 202–216.

Suzuki W, Yamada A, Aizawa R, Suzuki D, Kassai H, Harada T, Nakayama M, Nagahama R, Maki K, Takeda K, *et al.* (2015). Cdc42 is critical for cartilage development during endochondral ossification. Endocrinology 156, 314–322.

Terpstra L, Prud'homme J, Arabian A, Takeda S, Karsenty G, Dedhar S, St-Arnaud R (2003). Reduced chondrocyte proliferation and chondrodysplasia in mice lacking the integrin-linked kinase in chondrocytes. J Cell Biol 162, 139–148.

Walsh M, Connolly P, Jenkinson A, O'Brien T (2000). Leg length discrepancy—an experimental study of compensatory changes in three dimensions using gait analysis. Gait Posture 12, 156–161.

Wang G, Woods A, Agoston H, Ulici V, Glogauer M, Beier F (2007). Genetic ablation of rac1 in cartilage results in chondrodysplasia. Dev Biol 306, 612–623.

Ward KA, Caulton JM, Adams JE, Mughal MZ (2016). Perspective: cerebral palsy as a model of bone development in the absence of postnatal mechanical factors. J Musculoskelet Neuronal Interact 6, 154–159.

Wilsman NJ, Farnum CE, Leiferman EM, Fry M, Barreto C (1996). Differential growth by growth plates as a function of multiple parameters of chondrocytic kinetics. J Orthop Res 14, 927–936.

Woods A, Wang G, Beier F (2007). Regulation of chondrocyte differentiation by the actin cytoskeleton and adhesive interactions. J Cell Physiol 213, 1–8.